

Optical Far-Field Detection of Sub- $\lambda/14$ Wide Defects by Conjugate Structured Light-Field Microscopy (c-SIM)

Jinsong Zhang, Jiamin Liu, Hao Jiang, Jinlong Zhu,* and Shiyuan Liu*



Cite This: *ACS Photonics* 2023, 10, 3484–3493



Read Online

ACCESS |



Metrics & More

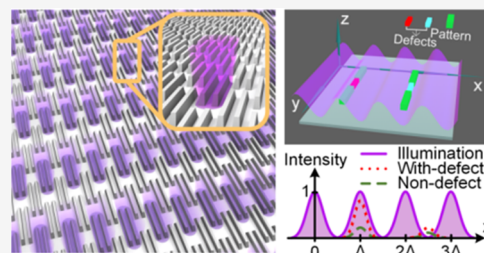


Article Recommendations



Supporting Information

ABSTRACT: Optical far-field detection and imaging of deep-subwavelength objects in a large-area wafer is challenging because of the well-known diffraction barrier and weak Rayleigh scattering. Although the scattering signal of deep subwavelength defects can be enhanced by various methods, such as using a high full-well-capacity camera and increasing the exposure time, the accurate classification of various defects and the precise positioning of defects in a subwavelength domain is rather challenging. In this letter, we report a theoretical framework that the optical bright-field imaging microscopy, coupled with an optical proximity correction-based structured light-field illumination mode, could pinpoint and classify various sub- $\lambda/14$ wide defects in a subwavelength domain in a large-area wafer. The underlying physics is that the illuminated structured light field, which is customized to mimic the geometrical feature of the background pattern in the wafer, creates the defect-induced breakdown of geometrical and electromagnetic symmetry. We believe that this work not only paves the route for optical wafer defect inspection and classification at advanced technology nodes but also could potentially be extended to many other areas, such as biosensing, lithographic mask inspection, material characterization, and nanoscale metrology.



KEYWORDS: far-field detection, defect inspection, structured light, patterned wafer, nanostructure

INTRODUCTION

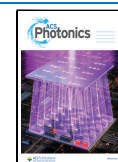
Integrated circuits (ICs) can nowadays be found in just about any modern piece of technology we can think of. Consumer electronics, data storage and processing, cars and transportation, medical instruments, robotics, home electronics, and security systems are stimulating the global demand for IC devices with high integration and low power consumption, which is the driving force for the fab to pursue high-volume and high-yield IC manufacturing at advanced nodes.¹ As the critical dimensions of transistors keep shrinking,^{2–5} there is a greater awareness that the defects induced by the fab may severely degrade the performance of IC devices.^{6–8} Hence, high-speed and high-sensitivity patterned wafer defect inspection is of great importance to the process control of IC manufacturing. Scanning electron microscopy,⁹ transmission electron microscopy,¹⁰ and atomic force microscopy^{11,12} could achieve single-digit nanometer resolution but suffer from the drawbacks of low efficiency and high-vacuum environment, making themselves unable to meet the requirements of IC in-line inspection.² In contrast, optical far-field microscopy-based inspection is intrinsically fast and non-destructive. Optical bright-field microscopy,¹³ diffraction phase microscopy,¹⁴ and optical pseudo-electrodynamics microscopy¹⁵ could achieve high-speed and large field-of-view (FOV) inspection of defects at advanced technology nodes (limited only by the frame rate and sensor size of a commercial camera). However, they are not able to classify different types

of deep subwavelength defects due to the diffraction barrier. As a result, the time-consuming and destructive e-beam inspection has to be used instead of optical inspection for defect classification.² Optical super-resolution imaging techniques, such as stimulated emission depletion microscopy^{16–19} and photothermal nonlinear confocal microscopy,²⁰ have the capability of imaging deep subwavelength nanostructures, but they require either fluorescence labeling or sample heating, which may pollute or damage the patterned wafer to some extent. Therefore, an optical far-field imaging method can not only inspect killer defects on the patterned wafer but also classify various types of defects in a fast, nondestructive, easy-of-operate, and large-FOV manner, which is of great importance to the field.

In this paper, we propose conjugate structured light-field microscopy (c-SIM) and theoretically demonstrate that c-SIM can accurately pinpoint and classify sub- $\lambda/14$ defects in a large-area nanoarray in a bright-field imaging mode. The term “conjugate” means that the amplitude distribution of the illuminated structured light field is well designed to precisely

Received: March 30, 2023

Published: September 6, 2023



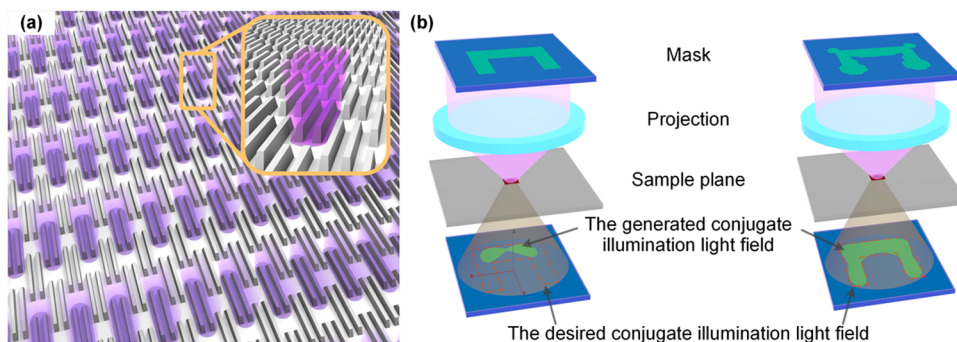


Figure 1. Schematic diagram of the generation of conjugate structured light field for patterned wafer defect inspection. (a) Schematic diagram of the proposed defect inspection strategy. A unit cell in the periodic sample consists of two parallel lines. For simplicity, the substrate and the pattern are all silica in our simulating experiments. As shown in the inset of (a), one sub-beam of the generated structured light field illuminates only a unit cell. A single line has 30 nm (top width) by 750 nm (bottom length) size. (b) A projection system akin to the one in optical lithography reproduces the pattern in the mask (SLM, DMD, or physical photomask) to the sample plane to generate the conjugate structured light field. The left and right schematics in (b) correspond to the same projection system but with different masks, *i.e.*, the initial and optimized (by the OPC method) masks. Apparently, the optimized mask results in an illumination pattern that retains the desired U shape, while the one that has an unoptimized mask cannot.

match the geometrical dimensions of the patterned nanostructures in the best focal plane, while the phase of the illuminated structured light field is not. We used the technique called optical proximity correction (OPC), which is adopted in optical lithography, to inversely design the conjugate structured light field that has features whose geometrical size is beyond the diffraction barrier.^{21,22} As the illuminated light field scans over the wafer surface (or vice versa), the scattering field of a defect in the far-field image switches back and forth between a dark mode and a bright mode, which enhances the contrast of the defect. It is the scanning of conjugate structured light illumination over the wafer surface that makes this technique capable of directly classifying deep subwavelength defects. Moreover, we found that the full width at half-maximum (FWHM) of the diffraction pattern of a defect obtained by our method is much smaller than that obtained by conventional bright-field microscopy.^{23,24} The aforementioned advantages make our method a potential solution to the contradiction between high-speed optical inspection and defect classification. Moreover, because the conjugate structured light field-based defect inspection is intrinsically a bright-field imaging method, we believe that it may also be utilized in other fields, such as biosensing, lithographic mask inspection, material characterization, and nanoscale metrology.

METHODOLOGY

In a conventional bright-field microscope, the illuminated field is approximately a plane wave in the whole FOV.²⁵ In this study, we use a conjugate structured light field, which is defined as the field whose amplitude distribution is well designed to precisely match the geometrical dimensions of the background nanopatterns, to illuminate the background nanopatterns using a 421 nm coherent source, after which the scattering field is captured by a bright-field microscope. We call this method c-SIM. Figure 1a depicts the principle of c-SIM, *i.e.*, a customized conjugate structured light field (in purple) instead of a plane wave illuminates the sample (in silver). The sample under inspection is an intentional defect array (IDA) wafer that consists of one type of line structure whose top width, bottom width, top length, bottom length, and height are 30 nm (about $\lambda/14$), 60, 650, 750, and 100 nm, respectively. The rectangular unit cell is 240 nm wide by 1000

nm long and contains 2 lines in the center, indicating a 60 nm line-to-line gap. In order to reduce the time consumption of rigorous electromagnetic simulation, we set the background pattern, defects, and substrate material as silica, whose complex refractive index is 1.468 at a wavelength of 421 nm. It is repeated in a rhombic lattice pattern to form a 2-dimensional array, as shown in Figure 1a. Therefore, the illumination light field should be designed to mimic the rhombic lattice pattern. The inset of Figure 1a is a zoomed-in view of a single sub-beam of the designed light field that illuminates the two lines in a single unit cell. For the sake of simplicity, the line structures in a unit cell are named twin lines. To inspect the whole patterned area, we scan the wafer by moving either the light field or the wafer, which can be physically achieved by a pair of scanning galvanometers or a piezoelectric ceramics driver. Because the illumination light field and the rhombic lattice pattern are geometrically symmetric, a defect can break the symmetry and, therefore, result in an observable scattering signal during the scanning. We will demonstrate that this signal could enable the precise positioning and classification of defects hereinafter. As of now, the remaining question is how to generate a conjugate illumination light field. In fact, if the sizes of the twin lines are larger than the illumination wavelength, the conjugate illumination light field can be easily generated by using a spatial light modulator (SLM), a digital micromirror device (DMD), or even a physical photomask. The schematic of a feasible experimental setup is shown in Figure S1. However, things get worse when the wavelength of the source is much larger than the size of twin lines (which is always the case in the scope of optical wafer defect inspection.^{26–28}), *i.e.*, the diffraction barrier starts to play the key role, leading to the severely distorted light field. To tackle this problem, we introduce the concept of OPC, which is a technique used in inverse lithography at advanced technology nodes, to our c-SIM. To the best of our knowledge, this is the first time OPC has been introduced in the scope of optical wafer defect inspection.

We use Figure 1b to illustrate the fundamental principle of OPC. In a projection lithography system,^{29–31} as shown in the left-hand side of Figure 1b, the input wavefront of the incident beam is modulated by an unoptimized mask pattern. Our goal is to generate a conjugate structured light field that reproduces

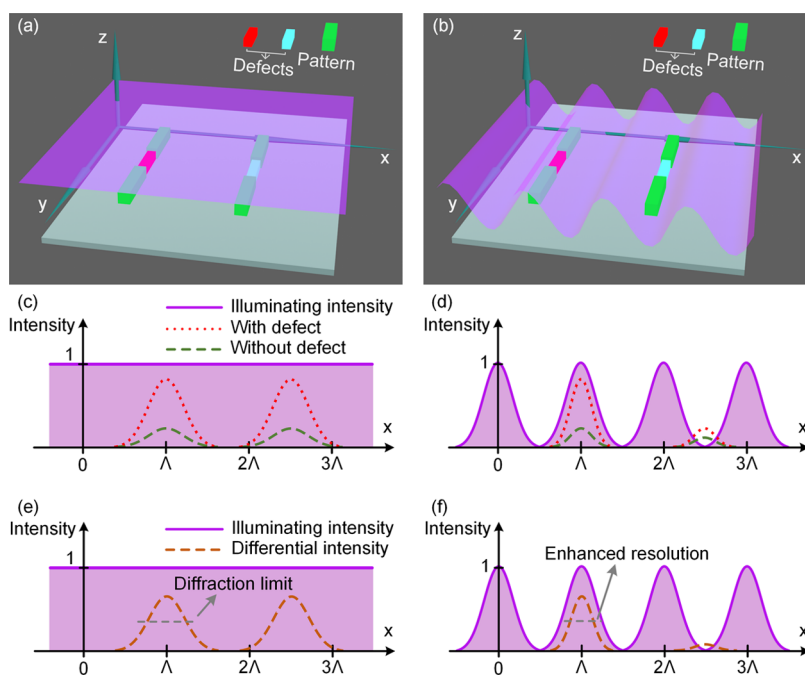


Figure 2. Underlying mechanism of high-precision positioning and enhanced resolution in c-SIM. The schematics in (a) and (b) denote the defective nanostructures under plane wave illumination and structured light-field illumination, respectively. (c) and (d) denote the cross-sections of the defect signals in the far-field images under plane wave illumination and conjugate structured light-field illumination, respectively. The red and blue defects (see subfigures (a) and (b)) have the same scattering intensity in (c), while the red defect has a stronger scattering intensity than that of the green defect in (d), indicating a higher positioning accuracy in c-SIM. (e) and (f) denote the differential intensity between the scattering intensity with and without defects under plane wave illumination and conjugate structured light-field illumination, respectively. The red and blue defects have the same intensity signals in (e), whose FWHMs are limited by the diffraction barrier. In contrast, the differential signal of the defect measured by c-SIM corresponds to a much narrower FWHM due to the conjugate structured light-field illumination, as shown in (f).

the mask pattern on the sample plane. However, because of the well-known diffraction barrier of light, the modulated wavefront, after passing through the entrance and exit pupils of the projection system, severely distorts, thus leading to a structured light field that biases significantly from the ideal mask pattern; see the left diagram in Figure 1b. To improve the resolution of the light field on the sample plane (i.e., to generate a conjugate structured light field that reproduces the shape of the target pattern), a simple but efficient method is to optimize the mask pattern by, for example, adding or deleting pixels around the original pattern. As a result, the distorted wavefront on the sample plane can be corrected by the added or deleted pixels on the mask, which is the core concept of OPC; see the right diagram in Figure 1b. The benefit is that we do not need to make any changes to the projection system, i.e., only the input photomask should be changed. This facilitates the simplification of the generation of the conjugate structured light field by using an SLM or a DMD, which could enable grayscale programming of the light field that is not achievable by a physical photomask. In order to implement OPC for generating the conjugate illumination light field, we use vectorial diffraction theory to rigorously model the propagation of the electromagnetic field in the projection system that has a high magnification factor and a high numerical aperture (NA).^{32,33} The intensity in the sample plane can be expressed as

$$I_{\text{image}} = \sum_{p=x,y,z} \|H_p \otimes M\|_2^2 \quad (1)$$

Here, H is the function of the projection system, M is a pixelated representation of the input mask pattern, and \otimes is

the symbol of two-dimensional convolution (see Section S2 for the unabridged description of the vector diffraction imaging theory). To inspect the deep subwavelength nanostructure, the feature size of the structured light field should be much smaller than the diffraction barrier. The OPC technique adjusts the input pixelated mask pattern M by minimizing the difference between the physically generated illumination field Z and the desired illumination light field M^* (i.e., the target pattern). The optimization can be formulated as the process of finding the minimum of a Frobenius norm F , i.e.,

$$F = \|Z - M^*\|_2^2 \quad (2)$$

To optimize the shape of the light field robustly, the imaging intensity I_{image} is translated to imaging pattern Z by using the Sigmoid function,²² which can be written as

$$Z = \frac{1}{1 + \exp(-a(I_{\text{image}} - b))} \quad (3)$$

Here, a is the steepness of the Sigmoid function, which affects the sensitivity in the iterative process, and b is the threshold for the binary projection of electromagnetic field intensity, which is critical to control the shape of the optimized light field. Due to the pattern's value being between zero and one, we convert it into an interval without boundaries by making use of a trigonometric function, i.e.,

$$M = \frac{1 + \cos \omega}{2}, \quad \omega \in (-\infty, +\infty) \quad (4)$$

Here, ω is the variable matrix corresponding to the input pattern M , which is used as an iterative target that is being

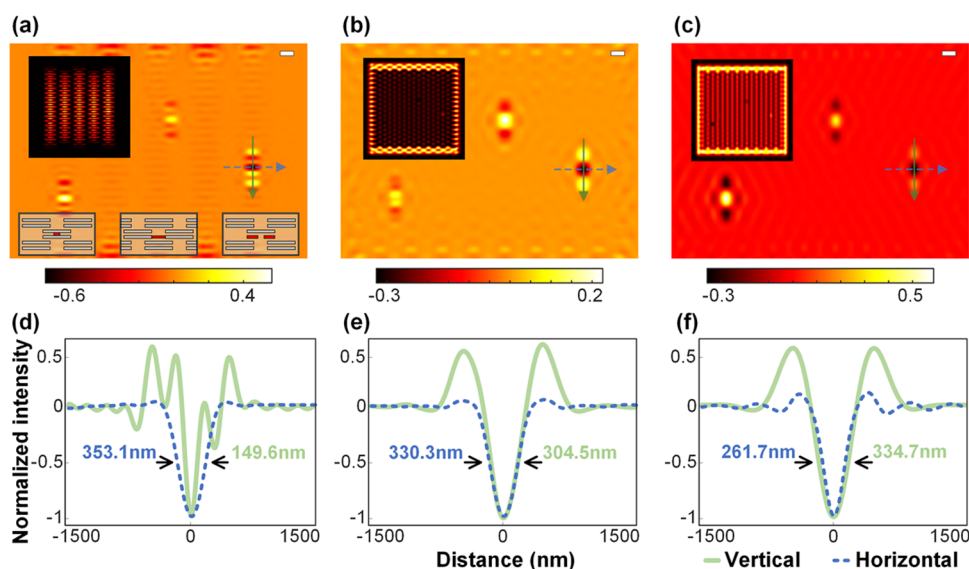


Figure 3. Defect inspection under different illuminating conditions. (a) The normalized second-order gradient image under the structured light-field illumination with horizontal polarization in c-SIM. The top inset shows the initial far-field image of the nanopattern with defects. The bottom insets depict three different defects investigated in the field-of-view, namely, the By bridge defect, the Bx bridge defect, and the Cutting defect. (b) and (c) are the normalized second-order gradient image in a conventional bright-field microscope under plane wave illumination with horizontal polarization and vertical polarization, respectively. The top insets in both subfigures show the initial far-field image of the nanopattern with defects. (d) The vertical and horizontal cross-sections correspond to the two arrows in (a), whose FWHMs are 149.6 and 351.3 nm, respectively. Notably, the FWHM in the vertical direction is much smaller than the diffraction barrier (270.3 nm). (e) The vertical and horizontal cross-sections correspond to the arrows in (b), whose FWHMs are 304.5 and 330.3 nm, respectively. (f) The vertical and horizontal cross-sections correspond to the arrows in (c), whose FWHMs are 334.7 and 261.7 nm, respectively. The scale bar is 500 nm.

updated in the iterative process. Then, we derive the gradient of the cost function F

$$\frac{\delta F}{\delta \omega} = 2a \cdot \sin(\omega) \cdot (H \otimes \{(Z - M^*) \cdot Z \cdot (1 - Z) \cdot (H \otimes M)\}) \quad (5)$$

M^* is the target pattern. In one iteration of the pattern optimization process, we first update the variable matrix ω , such as

$$\omega_{i+1} = \omega_i - \Delta \cdot \frac{\delta F}{\delta \omega_i} \quad (6)$$

Here, i is the iteration number and Δ is the step length. The updated input pattern is written as

$$M_{i+1} = (1 + \cos(\omega_i)) / 2 \quad (7)$$

Once F is less than a preset threshold, the iteration stops and outputs the optimal pattern M_{opt} (see Section S3 for the unabridged description of the OPC method). We can generate a structured light field with a feature size beyond the diffraction barrier (see Figure S4 for an application example of OPC) by utilizing OPC. The accuracy of positioning Ω of defects depends on the relative position between the structured light field and nanopattern. Therefore, the initial relative position between them needs to be found experimentally. Besides, the small feature size of the structured light field leads to a very sharp spatial variation of light intensity, which makes the switch of the defect's scattering pattern in the image faster and the change of the strength of perturbation in the far-field image corresponding to a defect more drastic in the scanning process. Therefore, we can accurately locate the defects with precision beyond the diffraction barrier. Based on the above analysis, the accuracy of positioning Ω is defined as

$$\Omega(x, y) \propto \|Z - M^*\|_2^2 \cdot \left(\frac{\delta I_{\text{image}}}{\delta x} + \frac{\delta I_{\text{image}}}{\delta y} \right) \quad (8)$$

where (x, y) denote the coordinates.

In addition to the capability of high-precision positioning of defects, the conjugate structured light field also enables far-field defect imaging with a higher resolution than its bright-field counterpart. We use two pairs of defective nanopatterns (bridge defects, marked in red and blue, as shown in Figure 2a,b) to illustrate the enhanced resolution. If the nanopattern is illuminated by a plane wave (as shown in Figure 2a), the two defects are both in bright mode and generate strong scattering intensity in the far-field, as shown by the red dashed line in Figure 2c. In Figure 2b, the defective nanopatterns are illuminated by a structured light field with sinusoidal distribution of amplitude along the x-direction. Due to the fact that the left defective nanopattern is placed in the peak of the structured light field, the red defect is in bright mode and thus generates a strong scattering intensity in far-field, as shown in Figure 2d. In contrast, the right defective nanopattern is placed in the valley of the structured light field; thus, the blue defect is in dark mode and corresponds to a weak scattering intensity in the far-field, as shown in Figure 2d. Hence, implementing the scanning of the OPC-optimized structured light field over the sample surface can achieve a higher accuracy of positioning than its plane wave illumination counterpart. The green dashed lines in Figure 2c,d corresponds to the cross-section of scattering intensity without defects. The differential intensity between the defective and defect-free nanopatterns obtained by plane wave and structured light-field illumination, as shown in Figure 2e,f, respectively, has demonstrated that the FWHM of the defect signal obtained by structured light-field illumination (the red dashed line in

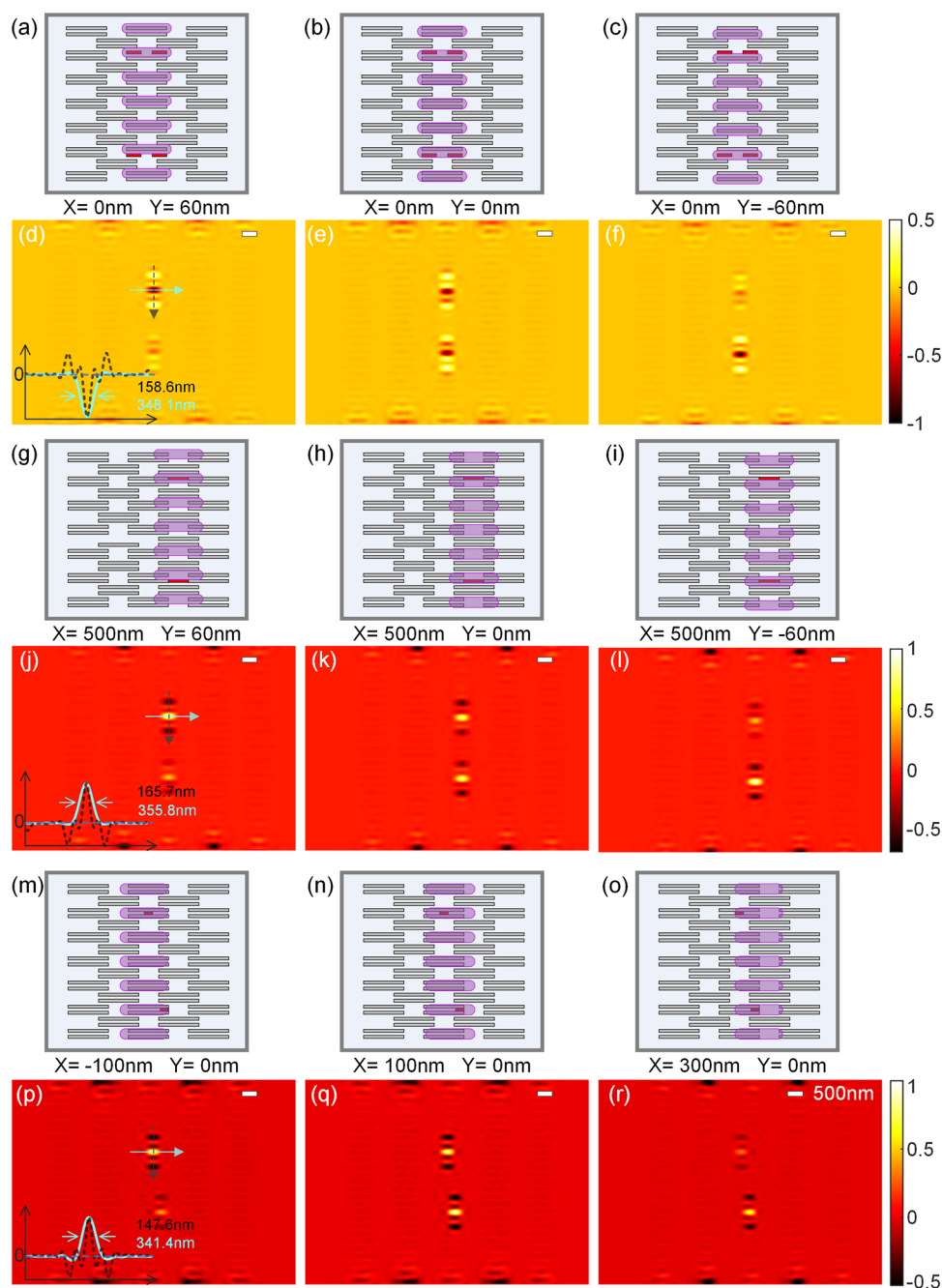


Figure 4. Defect inspection by scanning the wafer in the c-SIM. Cutting defect. (a–c) The coordinates of the illuminating beam with respect to the nanopattern are set as (0, 60 nm), (0, 0 nm), and (0, –60 nm), respectively. (d–f) The normalized second-order gradient images of the Cutting defect correspond to the three illumination positions in (a–c), respectively. Bx bridge defect. (g–i) The coordinates of the illuminating beam with respect to the nanopattern are set as (500, 60 nm), (500, 0 nm), and (500, –60 nm), respectively. (j–l) The normalized second-order gradient images of the Cutting defect that correspond to the three illumination positions in (g–i), respectively. By bridge defect. (m–o) The coordinates of the illuminating beam with respect to the nanopattern are set as (–100, 0 nm), (100, 0 nm), and (300, 0 nm), respectively. (p–r) The normalized second-order gradient images of the Cutting defect that correspond to the three illumination positions in (m–o), respectively. The insets in (d, j, p) demonstrate again that the diffraction barrier can be broken in c-SIM. Scale bar, 500 nm.

Figure 2f) is much smaller than the one obtained by plane wave illumination (the red dashed line in Figure 2e).

RESULTS AND DISCUSSION

After determining the spatial distribution of the structured light field and correcting for feature degradation (see Figure S5 for the generated structured light field conjugated with the tested nanopattern), we move on to consider the interaction between

the conjugated structured light field with the nanostructure in c-SIM. This includes the nanopattern in Figure 1, as well as various killer defects. To calculate the electromagnetic fields that interact with nonperiodic nanostructures, we employ the finite difference time domain (FDTD) method.^{34,35} We record the near-field, which does not include evanescent field backscattered by the nanostructure, using a monitor placed 400 nm above the nanostructure. Additionally, we utilize the vector diffraction imaging theory to calculate the far-field

microscopic image, which is typically captured by a detector in a bright-field microscope, corresponding to the near-field calculated by FDTD. The simulating parameters of the projection system are NA 0.95 and demagnification 100 \times .

In the preceding section, we have demonstrated how to determine the perturbation caused by the defect. This is achieved by computing the differential images between the far-field images obtained with and without defects. This process effectively isolates the scattering field of the defect from the background nanopattern, also avoiding any edge deterioration effects (see Figure S6 for the far-field images with defect, far-field images without defect, and differential images). However, capturing the reference image can be time-consuming, which is not ideal for real-time inspection. To address this limitation, we propose the computation of the second-order gradient image, which can be obtained using the following equation

$$G(x, y) = P(x, y + \tau) - 2P(x, y) + P(x, y - \tau) \quad (9)$$

Here, G represents the second-order gradient image, P denotes the initial far-field image at any illuminating position, and τ corresponds to the period of the image intensity along the y (vertical) direction.

We perform three comparative simulating measurements on the same IDA with different types of defects, using c-SIM with structured light-field illumination, as well as bright-field microscopy with horizontal and vertical polarization plane wave illumination. Our aim is to determine the sensitivity of different killer defects that are commonly found in periodic line/space nanostructures on pattern wafers. These killer defects include Cutting, By bridge, and Bx bridge,³⁶ as depicted in the bottom inset of Figure 3a. A stereoscopic view alongside the sizes of defects is shown in Figure S6. The top width, top length, bottom width, and bottom length of the Cutting defect are 30 nm (about $\lambda/14$), 250, 60, and 150 nm, respectively. The dimensions of the Bx bridge defect are 25 nm (less than $\lambda/14$), 350, 35, and 250 nm, respectively. The dimensions of the By bridge defect are 90, 100, 60, and 200 nm, respectively. The heights of the three defects are the same as that of the background pattern, i.e., 100 nm. To this end, we intentionally placed these defects discretely in a tested silica nanopattern on a silica substrate, as illustrated in Figure S6. For a specific illuminating position of the structured light field, the sub-beam of the structured light field is perfectly aligned with the twin lines, as shown in Figure 1a. This specific position of structured light is marked as $X = 0$ nm and $Y = 0$ nm using the center of twin lines as a reference. The simulating result of c-SIM shown in Figure 3a corresponds to the specific illuminating position with horizontal polarization. However, due to the edge deterioration in calculating the gradient image, the top and bottom sides of the normalized second-order gradient image are cut off. Nevertheless, all three types of defects produce corresponding perturbations in the initial far-field image, as demonstrated in the top inset of Figure 3a. After calculating the second-order gradient, we almost completely filtered out the scattering field of the background nanopattern, resulting in significant enhancement of the defects' perturbations. The perturbation strength of the Bx bridge defect is relatively weak for the sub-beam not aligned with it. In contrast, we conduct a c-SIM simulating measurement in the illumination position of $X = 500$ nm and $Y = 0$ nm, where the sub-beam aligns with the gap of the nanopattern. The corresponding result is shown Figure S6, which indicates a stronger perturbation caused by the Bx bridge defect. Figure 3d shows the cross-section of the

perturbation of the right Cutting defect in Figure 3a. The FWHMs are 149.6 and 353.1 nm in vertical and horizontal directions, respectively, which is beyond the diffraction-limited resolution $0.61 \lambda/\text{NA} = 270.3$ nm. On the other hand, with respect to the bright-field microscope with plane wave illumination of horizontal polarization and vertical polarization, the three types of defects generate unexpected and irregular perturbations in both the initial far-field image and normalized second-order gradient image, as depicted in Figure 3b,c. There are discernible distinctions between the two polarizations, particularly in terms of the direction of the elliptic perturbation, which is related to the polarization direction.

Moreover, the By bridge defect is more easily able to form a nanoantenna under illumination of the parallel electric field, rendering vertical polarization more sensitive to it.³⁷ The cross-section of the perturbation caused by horizontal polarization plane wave illumination is displayed in Figure 3e, where the FWHMs limited by the diffraction barrier in the vertical and horizontal directions are 304.5 and 330.3 nm, respectively. Likewise, the vertical polarization in Figure 3f exhibits FWHMs of 334.7 and 261.7 nm in vertical and horizontal directions, respectively. Despite the conjugate structured light field reducing the FWHMs of perturbations by approximately half compared to plane wave illumination, the perturbation is still too large to precisely position and classify defects. By leveraging the advantages of the structured light field, we modulate the breakdown induced by defects through the scanning of the relative position between the defects and the structured light field. This trick allows us to precisely identify the side on which a defect appears in relation to precisely identify the side on which a defect appears in relation to the twin lines.

To achieve accurate positioning and classify defects, we scan the relative position between defects and structured light field. As the strength of the defect-caused perturbation varies during the scanning process, a series of simulating measurements for c-SIM are conducted by scanning the illuminating position of the structured light field. Starting with the Cutting defect, we set a couple of axisymmetric Cutting defects on the different nanowires of twin lines in a large-scale ideal nanopattern, as shown in Figure S7. For the sake of presentation, Figure 4a is only a diagram of the defect's position and illuminating position. When the centers of the sub-beam of conjugate structured light field and twin lines are aligned perfectly, as shown in Figure 4b, both Cutting defects are simultaneously illuminated in the bright mode. The positive perturbations of the two Cutting defects in the second-order gradient image have similar strength, as shown in Figure 4e. Subsequently, we move the structured light upward to align it with the upper nanowire of the twin lines, as shown in Figure 4a. We observe a reverse change in the strength of the perturbations caused by the two Cutting defects, as depicted in Figure 4e, compared to Figure 4d. The upper Cutting defect causes a stronger perturbation due to this defect being at the center of the sub-beam and in bright mode. Its FWHMs in a set of orthogonal directions are 158.4 and 348.1 nm, which shows an enhanced resolution effect. Oppositely, the lower defect, in dark mode, produces a weaker perturbation. In the illuminating position shown in Figure 4c, the perturbations of two defects are reversed again, but the lower Cutting defect shows a stronger perturbation while the upper Cutting defect shows a weaker perturbation, as shown in Figure 4f. Moreover, differential images are produced by using far-field reference

images obtained from an ideal nanopattern without any defects, exhibiting the same phenomenon observed in the second-order gradient image, as illustrated in Figure S7. We find that the far-field scattering signal of the defect is stronger at the position where the sub-beam of the conjugate structured light field aligns with the nanowire containing the defect, indicating the fact that the defect-induced breaking of the symmetry of the electromagnetic field reaches its maximal value at this position. Therefore, we scan the relative position between the structured light field and defects to distinguish which nanowire of twin lines they are on.

Next, we perform a similar scanning operation for Bx bridge defects. In Figure S8, two Bx bridge defects are set on the different sides of the twin lines of a large-scale ideal nanopattern. We consider three illuminating positions of the conjugate structured light field where the center of the sub-beam is aligned with the upper side, center, and lower side of twin lines, as shown in Figure 4g–i, respectively. The perturbations of those defects exhibit similar evolutionary trends to the Cutting defect during the scanning operation, as shown in Figure 4j–l, respectively. The same evolutionary trends are revealed in the differential images, as shown in Figure S8. Therefore, we are able to distinguish on which nanowire of twin lines the Bx bridge defects are located. Besides, their perturbations in gradient images show a negative value, enabling us to distinguish them from Cutting defects. This evolutionary trend can be summarized as the strength of perturbations becoming weaker as the defects gradually transform from the bright mode to the dark mode when the sub-beam moves away from the defects. The set of FWHMs of the upper perturbation in Figure 4j are 165.7 and 355.8 nm, which is beyond the diffraction-limited resolution.

Finally, we consider the By bridge defect. We place a defect in the center of the twin lines and another on the right side of the twin lines in an ideal nanopattern, as shown in Figure S9. The negative perturbations of two By bridge defects have a slight misalignment in the vertical direction, which is consistent with the misalignment of the two By bridge defects. Due to the significant difference in the dimensions of the twin lines between the horizontal direction and vertical direction, we can roughly locate on which side of the twin lines the position of the By bridge defect is, based on the absolute position of negative perturbation in the gradient image. Moreover, we can accurately locate the By bridge defects by using the same scanning operator as the other two types of defects. To do this, we scan the structured light field along the horizontal direction due to the possible location of this defect being in this direction, as shown in Figure 4m–o, respectively. The negative perturbations of By bridge defects exhibit the same evolutionary trend, as shown in Figure 4p–r, respectively. Figure S9 shows the same phenomenon by calculating the differential images. Consequently, we can distinguish the By bridge defects on different sides of twin lines either by the gradient image or by the scanning operator. Besides, the FWHMs of the upper perturbation in Figure 4p are 147.6 and 341.4 nm, which is about half of the diffraction-limited resolution.

To evaluate the precision of defect localization of the proposed method, we scan the illumination position of the structured light field over the wafer surface with an even smaller step size of 5 nm, followed by calculating the defect-induced far-field scattering signal as a function of the scanning positions. We first employed the unoptimized initial structured

light field for illumination, as shown in Figure S10a. The more pronounced variations of the sub-beams in the initial structured light field along the horizontal direction result in a more significant change in the far-field signal of defects during the scanning process, leading to higher sensitivity and precision. It is of great importance to note that the Cutting and Bx bridge defects in the background nanopatterns must disrupt the local structure's symmetry. As a result, this may lead to the fact that the strongest scattering signals of defects do not align with the defect's physical center even when the sub-beam is perfectly aligned with the center of defects (as illustrated in Figure S10). We took the By bridge defect inspection as an example: we scanned the structured light field along X and Y directions over the wafer surface, respectively. First, we performed the scanning along the X-direction from −200 to 500 nm with a step size of 5 nm while keeping the Y position fixed. The far-field scattering signal of Defect 1 (i.e., the upper By bridging defect) is the strongest at $X = 0$ nm, indicating a perfect alignment with the physical center of Defect 1, as depicted by the blue solid line in Figure 5. The far-

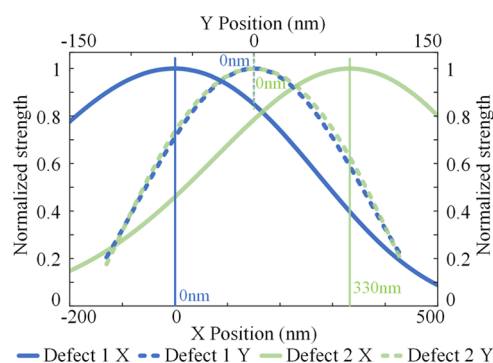


Figure 5. Normalized far-field scattering signal of By bridge defects as a function of the position of the scanning structured light field. Defect 1 and Defect 2 correspond to the upper and lower By bridging defects in Figure 4m, respectively. The blue and green curves represent Defect 1 and Defect 2, respectively. The solid and dashed curves represent the X and Y directions, respectively. The vertical lines mark the positions of the maximal value.

field scattering signal of Defect 2 (i.e., the lower By bridging defect) reaches its maximum at $X = 330$ nm (see the green solid line in Figure 5), which deviates from the physical center of Defect 2 (i.e., at 275 nm) by 55 nm. We then performed the scanning along the Y-direction from −120 to 120 nm with a step size of 5 nm while keeping the X position fixed. As expected, the strongest perturbations caused by both Defect 1 and Defect 2 appear at the position of $Y = 0$ nm, perfectly aligning with the physical center of the defects. This deviation in the X scanning may be attributed to the off-axis scattering of defects in the pattern as long as the defect–pattern–substrate coupling, which is widely seen in optics-based patterned wafer defect inspection.^{15,36} Moreover, we should emphasize that although the maximum of the far-field scattering signal of the killer defects may deviate from the defect's physical center, it does not hinder the capability of our proposed method to determine which side of the unit cell the defect is located at.

After demonstrating the advantages of the proposed theoretical framework by conducting a series of simulations, it is of great importance to assess the feasibility of this method. We have presented the optimized mask pattern with a grid size of 10 nm, as shown in Figure S5. Due to the utilization of a

projection system with a demagnification factor of 100 \times , the actual grid size of the mask is 1 μm , which can be easily realized by fabricating a physical photomask with state-of-the-art E-beam lithography tools. Therefore, it is feasible to generate conjugate structured light-field illumination in practice. Besides, we also used the same grid size, 10 nm, for the mask pattern, which corresponds to a grid size of 1 μm in the image space, for the calculation of the far-field images. This allows us to theoretically compute the FWHMs of the defect signals more accurately. In future experiments, we will consider the balance between the pixel size and signal-to-noise ratio (SNR) of off-the-shelf cameras. For example, we can easily find a scientific camera with pixel sizes ranging from 2 to 3 μm (for instance, BFS-U3-200S7M-C, FLIR) to characterize a 150 nm-wide (i.e., the FWHM) defect signal, which corresponds to 15 μm in the image space after using a 100 \times microscope. In conclusion, we believe that the generation of the conjugate structured light field and the collection of the far-field images of the defects are both feasible in practice using the proposed c-SIM.

Benefiting from the optimized conjugate structured light field in c-SIM matched with the tested ideal nanopattern, potential unwanted defects in the tested ideal nanopattern will disrupt the electromagnetic symmetry. During the scanning process, defect-induced perturbations vary in strength as the defects switch between bright and dark modes. With the help of the relative position of the defects and structured light field, we can now accurately locate the three killer defects on either side of the twin lines, even when the positions of the defects are not very clear from the second-order gradient image or differential image alone. The accuracy of localizing defects of c-SIM also depends on the accuracy of scanning the structured light field in a real-world experiment, which can achieve scanning accuracy of several nanometers by using a piezoelectric ceramic driver. The Cutting and By bridge defects have opposite perturbation values in the gradient images and differential images, which allows them to be easily distinguished from each other. Additionally, both types of defects show higher sensitivity when the sub-beam is aligned with the twin lines, which makes it easier to detect their presence. Conversely, only the Bx bridge defect is sensitive when the sub-beam is aligned with the gap space of the ideal nanopattern (see Figure S6). This characteristic makes it easy to distinguish the Bx bridge defect from the other two types of defects. Nevertheless, determining the illuminating position of the structured light field for c-SIM in real-world experiments poses a considerable challenge. Fortunately, the far-field images of different illuminating positions exhibit distinct characteristics. One possible approach is to precalculate the far-field images in two (three or more) specific illuminating positions, such as the sub-beam perfectly aligns with the center of the twin lines and the gap space of the nanopattern, as shown in Figure 4b,h, respectively. Subsequently, we can experimentally find the two special illuminating positions based on the far-field image captured by a detector. Our theoretical investigation has demonstrated that c-SIM can be implemented in practice for enhanced defect detection.

CONCLUSIONS

In summary, we have used rigorous electromagnetic simulations to validate the capability of c-SIM in the inspection of deep subwavelength defects in a background pattern. Compared to traditional bright-field microscopy-based defect

inspection, c-SIM inspects the sample using a customized structured light field by an OPC technique to match the geometry of the background nanopattern on the sample. Any defect in the background nanopattern breaks the geometrical and light-field symmetry. As a result, we can precisely determine on which side of the twin lines the defect is located (i.e., a unit cell of the background nanopattern in this paper) by scanning the structured light field, which is not achievable by conventional bright-field microscopes. Moreover, because c-SIM utilizes an OPC-designed structured light field for illumination, the scattering pattern of defects heavily depends on the type of defect and the illuminating position. As a result, we can classify multiple types of defects through a simple linear scanning of the structured light field over the sample surface (or vice versa). Last but not least, the smallest FWHM of the defect signal is about one-third of the wavelength λ , way smaller than the diffraction limit of the coherent inspection system. The enhanced resolution improves the accuracy of defect positioning without any additional scanning. Here, we should clarify the significant differences among c-SIM, structured illumination microscopy (SIM),^{24,38–40} and light-field microscopy (LFM).^{41–43} First of all, c-SIM requires the customized coherent illumination field to match the nanostructures under measurement, while LFM and SIM typically utilize moiré fringes and plane wave illumination, respectively. Second, OPC is introduced in c-SIM to customize the illumination field with features beyond the diffraction limit, while SIM and LFM do not. Last but not least, c-SIM requires prior knowledge of the sample in order to customize the illumination field and implement the scanning strategy, while SIM and LFM are typically sample-independent. As a result, c-SIM is more suitable for the imaging and metrology of artificial samples. In summary, we believe that our theoretical framework advances the scope of patterned wafer defect inspection by combining OPC, structured light-field illumination, and bright-field microscopy. Moreover, because c-SIM is inherently a bright-field imaging technique and does not require any sample preparation procedure, we believe that this technique potentially provides a new route for many other applications, such as bioimaging, lithographic mask inspection, microbiology, and nanoscale metrology.

ASSOCIATED CONTENT

Supporting Information

The Supporting Information is available free of charge at <https://pubs.acs.org/doi/10.1021/acsphotonics.3c00434>.

Simplified experimental configuration; vector diffraction imaging theory; OPC method and application example; generated structured light field; simulating nanopattern; optical inspection for three different types of defects; and optical far-field classification of two Cutting defects, two Bx bridge defects, and two By bridge defects by the differential images (PDF)

AUTHOR INFORMATION

Corresponding Authors

Jinlong Zhu — State Key Laboratory of Digital Manufacturing Equipment and Technology, Huazhong University of Science and Technology, Wuhan 430074, China; orcid.org/0000-0002-5723-2879; Email: jinlongzhu03@hust.edu.cn

Shiyuan Liu — State Key Laboratory of Digital Manufacturing Equipment and Technology, Huazhong University of Science

and Technology, Wuhan 430074, China; orcid.org/0000-0002-0756-1439; Email: shyliu@hust.edu.cn

Authors

Jinsong Zhang – State Key Laboratory of Digital Manufacturing Equipment and Technology, Huazhong University of Science and Technology, Wuhan 430074, China

Jiamin Liu – State Key Laboratory of Digital Manufacturing Equipment and Technology, Huazhong University of Science and Technology, Wuhan 430074, China

Hao Jiang – State Key Laboratory of Digital Manufacturing Equipment and Technology, Huazhong University of Science and Technology, Wuhan 430074, China; orcid.org/0000-0003-0561-5058

Complete contact information is available at:

<https://pubs.acs.org/10.1021/acsphotonics.3c00434>

Author Contributions

This concept was built by J. Zhu. The OPC optimization and near-field calculation programs were developed by J. Zhang. The vector diffracted imaging theory was derived by J. Zhang and J.L. J. Zhu and S.L. supervised the project. All the authors discussed the results and commented on the manuscript and have given approval to the final version of the manuscript.

Notes

The authors declare no competing financial interest.

ACKNOWLEDGMENTS

The authors would like to thank the support from the National Nature Science Foundation of China (Grant Nos. 52175509 and 52130504), the National Key Research and Development Program of China (2017YFF0204705), and the 2021 Postdoctoral Innovation Research Plan of Hubei Province (0106100226).

REFERENCES

- (1) International Roadmap for Devices and Systems (IRDS). <https://irds.ieee.org/editions/2020> (accessed March 08, 2023).
- (2) Orji, N. G.; Badaroglu, M.; Barnes, B. M.; Beitia, C.; Bunday, B. D.; Celano, U.; Kline, R. J.; Neisser, M.; Obeng, Y.; Vldar, A. E. Metrology for the Next Generation of Semiconductor Devices. *Nat. Electron.* **2018**, *1*, 532–547.
- (3) Vogel, E. Technology and Metrology of New Electronic Materials and Devices. *Nat. Nanotechnol.* **2007**, *2*, 25–32.
- (4) Zhu, J.; Udupa, A.; Goddard, L. L. Visualizable Detection of Nanoscale Objects Using Anti-Symmetric Excitation and Non-Resonance Amplification. *Nat. Commun.* **2020**, *11*, No. 2754.
- (5) Hasan, R. M. M.; Luo, X. Promising Lithography Techniques for Next-Generation Logic Devices. *Nanomanuf. Metrol.* **2018**, *1*, 67–81.
- (6) Urita, K.; Sato, Y.; Suenaga, K.; Gloter, A.; Hashimoto, A.; Ishida, M.; Shimada, T.; Shinohara, H.; Iijima, S. Defect-Induced Atomic Migration in Carbon Nanopeapod: Tracking the Single-Atom Dynamic Behavior. *Nano Lett.* **2004**, *4*, 2451–2454.
- (7) Kalbac, M.; Hsieh, Y. P.; Farhat, H.; Kavan, L.; Hofmann, M.; Kong, J.; Dresselhaus, M. S. Defects in Individual Semiconducting Single Wall Carbon Nanotubes: Raman Spectroscopic and in Situ Raman Spectroelectrochemical Study. *Nano Lett.* **2010**, *10*, 4619–4626.
- (8) Barnes, B. M.; Sohn, M. Y.; Goasmat, F.; Zhou, H.; Vldar, A. E.; Silver, R. M.; Arceo, A. Three-Dimensional Deep Sub-Wavelength Defect Detection Using $\lambda = 193$ nm Optical Microscopy. *Opt. Express* **2013**, *21*, 26219–26226.
- (9) Frase, C. G.; Buhr, E.; Dirscherl, K. Cd Characterization of Nanostructures in Sem Metrology. *Meas. Sci. Technol.* **2007**, *18*, S10–S19.
- (10) Ophus, C. Four-Dimensional Scanning Transmission Electron Microscopy (4d-Stem): From Scanning Nanodiffraction to Ptychography and Beyond. *Microsc. Microanal.* **2019**, *25*, S63–S82.
- (11) Hussain, D.; Ahmad, K.; Song, J.; Xie, H. Advances in the Atomic Force Microscopy for Critical Dimension Metrology. *Meas. Sci. Technol.* **2017**, *28*, No. 012001.
- (12) Dai, G.; Hahm, K.; Scholze, F.; Henn, M.-A.; Gross, H.; Fluegge, J.; Bosse, H. Measurements of Cd and Sidewall Profile of EUV Photomask Structures Using Cd-AFM and Tilting-AFM. *Meas. Sci. Technol.* **2014**, *25*, No. 044002.
- (13) Lugagne, J. B.; Jain, S.; Ivanovitch, P.; Ben Meriem, Z.; Vulin, C.; Fracassi, C.; Batt, G.; Hersen, P. Identification of Individual Cells from Z-Stacks of Bright-Field Microscopy Images. *Sci. Rep.* **2018**, *8*, No. 11455.
- (14) Zhou, R.; Edwards, C.; Arbabi, A.; Popescu, G.; Goddard, L. L. Detecting 20 nm Wide Defects in Large Area Nanopatterns Using Optical Interferometric Microscopy. *Nano Lett.* **2013**, *13*, 3716–3721.
- (15) Zhu, J.; Liu, Y.; Yu, X.; Zhou, R.; Jin, J. M.; Goddard, L. L. Sensing Sub-10 nm Wide Perturbations in Background Nanopatterns Using Optical Pseudoelectrodynamics Microscopy (Opem). *Nano Lett.* **2019**, *19*, 5347–5355.
- (16) Betzig, E.; Patterson, G.; Sougrat, R.; Lindwasser, O.; Olenych, S.; Bonifacino, J.; Davidson, M.; Lippincott-Schwartz, J.; Hess, H. Imaging Intracellular Fluorescent Proteins at Nanometer Resolution. *Science* **2006**, *313*, 1642–1645.
- (17) Rittweger, E.; Han, K. Y.; Irvine, S. E.; Eggeling, C.; Hell, S. W. STED Microscopy Reveals Crystal Colour Centres with Nanometric Resolution. *Nat. Photonics* **2009**, *3*, 144–147.
- (18) Willig, K. I.; Rizzoli, S. O.; Westphal, V.; Jahn, R.; Hell, S. W. STED Microscopy Reveals That Synaptotagmin Remains Clustered after Synaptic Vesicle Exocytosis. *Nature* **2006**, *440*, 935–939.
- (19) Nguyen, D. T.; Mun, S.; Park, H.; Jeong, U.; Kim, G. H.; Lee, S.; Jun, C. S.; Sung, M. M.; Kim, D. Super-Resolution Fluorescence Imaging for Semiconductor Nanoscale Metrology and Inspection. *Nano Lett.* **2022**, *22*, 10080–10087.
- (20) Zhang, T.; Che, Y.; Chen, K.; Xu, J.; Xu, Y.; Wen, T.; Lu, G.; Liu, X.; Wang, B.; Xu, X.; Duh, Y. S.; Tang, Y. L.; Han, J.; Cao, Y.; Guan, B. O.; Chu, S. W.; Li, X. Anapole Mediated Giant Photothermal Nonlinearity in Nanostructured Silicon. *Nat. Commun.* **2020**, *11*, No. 3027.
- (21) Lv, W.; Liu, S.; Xia, Q.; Wu, X.; Shen, Y.; Lam, E. Y. Level-Set-Based Inverse Lithography for Mask Synthesis Using the Conjugate Gradient and an Optimal Time Step. *J. Vac. Sci. Technol. B* **2013**, *31*, No. 041605.
- (22) Lv, W.; Xia, Q.; Liu, S. Mask-Filtering-Based Inverse Lithography. *J. Micro/Nanolithogr., MEMS, MOEMS* **2013**, *12*, No. 043003.
- (23) Huang, X.; Fan, J.; Li, L.; Liu, H.; Wu, R.; Wu, Y.; Wei, L.; Mao, H.; Lal, A.; Xi, P.; Tang, L.; Zhang, Y.; Liu, Y.; Tan, S.; Chen, L. Fast, Long-Term, Super-Resolution Imaging with Hessian Structured Illumination Microscopy. *Nat. Biotechnol.* **2018**, *36*, 451–459.
- (24) Wu, Y.; Shroff, H. Faster, Sharper, and Deeper: Structured Illumination Microscopy for Biological Imaging. *Nat. Methods* **2018**, *15*, 1011–1019.
- (25) Migliozi, D.; Zhao, B.; Gijs, M. A. M. 3d Nanometrology of Transparent Objects by Phase Calibration of a Basic Bright-Field Microscope for Multiple Illumination Apertures. *Opt. Express* **2020**, *28*, 28882–28895.
- (26) Yoon, J. W.; Ma, S.-M.; Kim, G. P.; Kang, Y.; Hahn, J.; Kwon, O.-J.; Kim, K.; Song, S. H. Nanophotonic Identification of Defects Buried in Three-Dimensional NAND Flash Memory Devices. *Nat. Electron.* **2018**, *1*, 60–67.
- (27) Virk, K. S. Fast Computation of Scattering by Isolated Defects in Periodic Dielectric Media. *J. Opt. Soc. Am. B* **2021**, *38*, 1763–1775.
- (28) Barnes, B. M.; Henn, M.-A.; Sohn, M. Y.; Zhou, H.; Silver, R. M. Assessing Form-Dependent Optical Scattering at Vacuum- and

Extreme-Ultraviolet Wavelengths of Nanostructures with Two-Dimensional Periodicity. *Phys. Rev. Appl.* **2019**, *11*, No. 064056.

(29) Sanders, D. P. Advances in Patterning Materials for 193 Nm Immersion Lithography. *Chem. Rev.* **2010**, *110*, 321–360.

(30) van Schoot, J.; van Setten, E.; Kaiser, W.; Neumann, J. T.; Migura, S.; Kneer, B.; Troost, K. Z.; Rispens, G. High-Numerical Aperture Extreme Ultraviolet Scanner for 8-Nm Lithography and Beyond. *J. Micro/Nanolithogr., MEMS, MOEMS* **2017**, *16*, No. 041010.

(31) Ito, T.; Okazaki, S. Pushing the Limits of Lithography. *Nature* **2000**, *406*, 1027–1031.

(32) Kim, J.; Wang, Y.; Zhang, X. Calculation of Vectorial Diffraction in Optical Systems. *J. Opt. Soc. Am. A* **2018**, *35*, 526–535.

(33) Erdmann, A.; Evanschitzky, P. Rigorous Electromagnetic Field Mask Modeling and Related Lithographic Effects in the Low K1 and Ultrahigh Numerical Aperture Regime. *J. Micro/Nanolithogr., MEMS, MOEMS* **2007**, *6*, No. 031002.

(34) Kunz, K. S.; Luebbers, R. J. *The Finite Difference Time Domain Method for Electromagnetics*; CRC Press, 1993.

(35) Golani, O.; Dolev, I.; Pond, J.; Niegemann, J. Simulating Semiconductor Structures for Next-Generation Optical Inspection Technologies. *Opt. Eng.* **2016**, *55*, No. 025102.

(36) Zhu, J.; Liu, J.; Xu, T.; Yuan, S.; Zhang, Z.; Jiang, H.; Gu, H.; Zhou, R.; Liu, S. Optical Wafer Defect Inspection at the 10 Nm Technology Node and Beyond. *Int. J. Extreme Manuf.* **2022**, *4*, No. 032001.

(37) Giannini, V.; Fernandez-Dominguez, A. I.; Heck, S. C.; Maier, S. A. Plasmonic Nanoantennas: Fundamentals and Their Use in Controlling the Radiative Properties of Nanoemitters. *Chem. Rev.* **2011**, *111*, 3888–3912.

(38) Ströhl, F.; Kaminski, C. F. Frontiers in Structured Illumination Microscopy. *Optica* **2016**, *3*, 667–677.

(39) Saxena, M.; Eluru, G.; Gorthi, S. S. Structured Illumination Microscopy. *Adv. Opt. Photonics* **2015**, *7*, 241–275.

(40) Schermelleh, L.; Carlton, P. M.; Haase, S.; Shao, L.; Winoto, L.; Kner, P.; Burke, B.; Cardoso, M. C.; Agard, D. A.; Gustafsson, M. G. L.; Leonhardt, H.; Sedat, J. W. Subdiffraction Multicolor Imaging of the Nuclear Periphery with 3d Structured Illumination Microscopy. *Science* **2008**, *320*, 1332–1336.

(41) Xiong, B.; Zhu, T.; Xiang, Y.; Li, X.; Yu, J.; Jiang, Z.; Niu, Y.; Jiang, D.; Zhang, X.; Fang, L.; Wu, J.; Dai, Q. Mirror-Enhanced Scanning Light-Field Microscopy for Long-Term High-Speed 3d Imaging with Isotropic Resolution. *Light: Sci. Appl.* **2021**, *10*, 227.

(42) Guo, C.; Liu, W.; Hua, X.; Li, H.; Jia, S. Fourier Light-Field Microscopy. *Opt. Express* **2019**, *27*, 25573–25594.

(43) Li, H.; Guo, C.; Kim-Holzappel, D.; Li, W.; Altschuller, Y.; Schroeder, B.; Liu, W.; Meng, Y.; French, J. B.; Takamaru, K. I.; Frohman, M. A.; Jia, S. Fast, Volumetric Live-Cell Imaging Using High-Resolution Light-Field Microscopy. *Biomed. Opt. Express* **2019**, *10*, 29–49.

Supporting Information

Optical Far-Field Detection of Sub- $\lambda/14$ Wide Defects by Conjugate Structure Light-Field Microscopy (c-SIM)

*Jinsong Zhang,^a Jiamin Liu,^a Hao Jiang,^a Jinlong Zhu,^{*a} Shiyuan Liu^{*a}*

^aState Key Laboratory of Digital Manufacturing Equipment and Technology, Huazhong University of Science and Technology, Wuhan 430074, China

**Email: jinlongzhu03@hust.edu.cn; shyliu@hust.edu.cn*

Contents:

S1. The simplified experimental configuration of the proposed c-SIM.

(Figure S1)

S2. Vector diffraction imaging theory. (Figure S2)

S3. Optical proximity correction method. (Figure S3)

S4. An application example of OPC. (Figure S4)

S5. The generated structured light field by OPC. (Figure S5)

S6. Optical inspection for three different types of defects. (Figure S6)

S7. Optical far-field classification of two Cutting defects with opposite orientation. (Figure S7)

S8. Optical far-field classification of two Bx bridge defects with opposite orientation. (Figure S8)

S9. Optical far-field classification of two By bridge defects with opposite orientation. (Figure S9)

S10. Defect localization precision. (Figure S10)

S1. The simplified experimental configuration of the proposed c-SIM

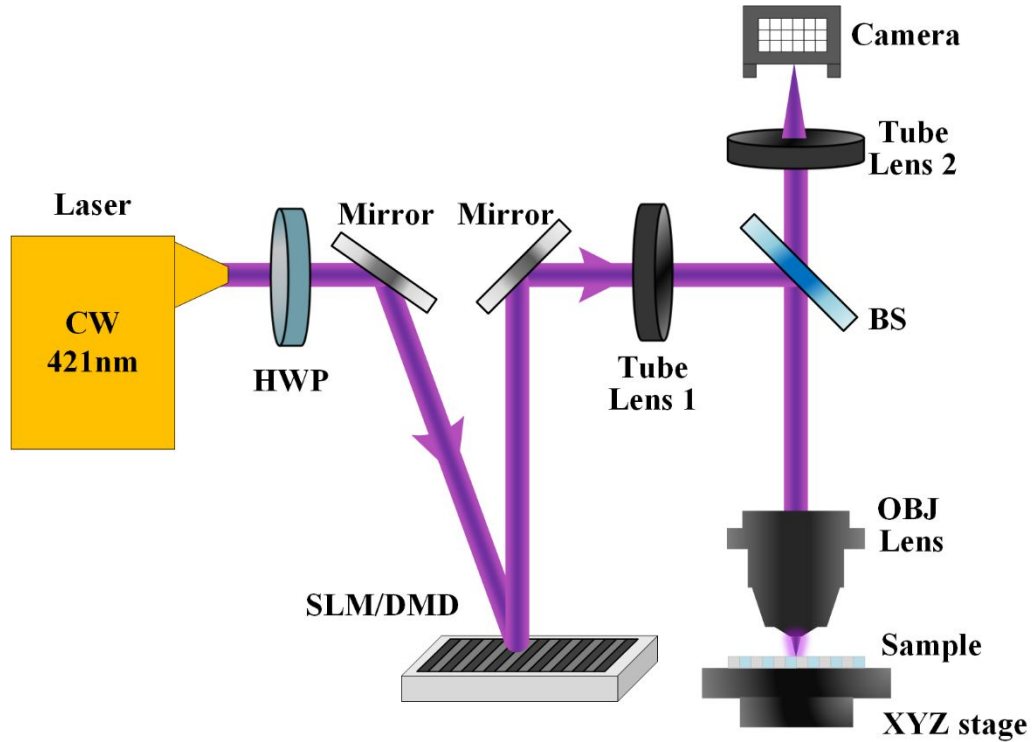


Figure S1 The simplified experimental configuration of the proposed conjugate structure light-field microscopy (c-SIM).

A simplified experimental configuration of the proposed c-SIM is shown in Fig. S1. We used a continuous-wave laser with a central wavelength of 421 nm as the system's light source in our simulated experiment. A half-wave plate is used to adjust the polarization angle of the illumination beam. The SLM or DMD is used to create the optimal structured light in the sample plane by loading an optimal mask pattern that is generated by our in-house developed OPC algorithm. Tube lens 1 and the objective constitute a projection system that projects the wavefront (i.e., the conjugate structure light field) modulated by SLM/DMD into the sample plane for illumination. The scattering field of the sample is then collected by the same objective followed by the projection of tube lens 2 to the camera. In order to implement the scanning procedure, the sample can be mounted on a motorized translation stage or the illumination beam can be rapidly adjusted by a scanning galvanometer.

S2. Vector diffraction imaging theory

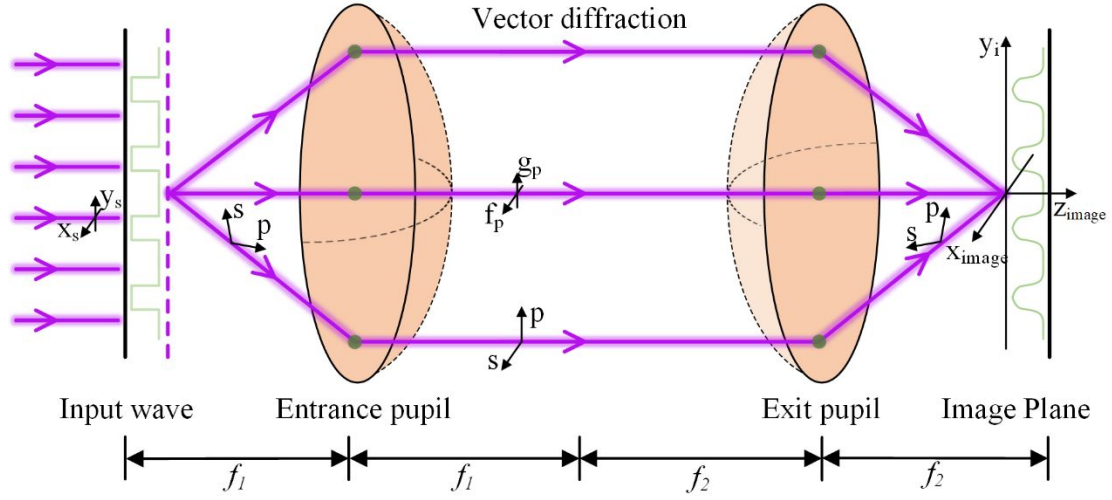


Figure S2 Schematic diagram of the projection system and the vector diffraction theory. The light beam radiated by the source passes through the mask and forms the input wave of the projection system. Then, the input wave passes through the projection system and generates an image in the image plane.

The electric field of the source is described as

$$E_S = \begin{bmatrix} E_{S-x} & E_{S-y} & E_{S-z} \end{bmatrix}^T, \quad (S1)$$

where E_S , E_{S-x} , E_{S-y} , E_{S-z} denote different polarization states, and T denotes the matrix transpose. We use thin mask approximation to model the transmission function of the mask. The electric field after the mask can be written as

$$E_{in} = M \cdot \begin{bmatrix} E_{S-x} & E_{S-y} & E_{S-z} \end{bmatrix}^T. \quad (S2)$$

To implement vectorial computation, the coordinates in the frequency domain of the pupil plane can be written as

$$\begin{aligned} \alpha_{en} &= \sin \theta_{in} \cos \varphi_{in}, & \beta_{en} &= \sin \theta_{in} \sin \varphi_{in}, & \gamma_{en} &= \cos \theta_{in} \\ \alpha_{ex} &= \frac{\alpha_{en}}{m}, & \beta_{ex} &= \frac{\beta_{en}}{m}, & \gamma_{ex} &= \sqrt{1 - \alpha_{ex}^2 - \beta_{ex}^2}. \end{aligned} \quad (S3)$$

Here, θ_{in} and φ_{in} are the incident angle and azimuth angle of the wave vector of the incident wave. α , β , and γ are the positions of the light beam in the frequency domain, where the subscript *en* and *ex* represent the entrance pupil plane and exit pupil plane,

respectively. m is the demagnification of the projection system. The electric field in the entrance pupil plane E_{en} can be expressed as

$$E_{en}(\alpha_{en}, \beta_{en}, \gamma_{en}) = T_{en} \cdot \frac{\gamma_{en}}{j \cdot \lambda} \cdot \frac{\exp(j \cdot 2\pi \cdot r_{en})}{r_{en}} \cdot f(E_{in}) \cdot W(\alpha_{en}, \beta_{en}). \quad (S4)$$

Here, r_{en} is the distance between the source point in the input pattern and the image point in the entrance pupil plane. $f()$ denotes the two-dimension Fourier transform. $W()$ denotes the window function of the projection system that can be expressed as

$$W = \begin{cases} 1 & (\alpha_{en}^2 + \beta_{en}^2) / (NA \cdot m)^2 \leq 1 \\ 0 & \text{others} \end{cases}. \quad (S5)$$

Here T_{en} is the transformational matrix from global coordinates to the local coordinate, which can be written as

$$T_{en} = \begin{bmatrix} \frac{-\beta_{en}}{\sqrt{\alpha_{en}^2 + \beta_{en}^2}} & \frac{\alpha_{en}}{\sqrt{\alpha_{en}^2 + \beta_{en}^2}} \\ \frac{-\alpha_{en}}{\gamma_{en} \cdot \sqrt{\alpha_{en}^2 + \beta_{en}^2}} & \frac{-\beta_{en}}{\gamma_{en} \cdot \sqrt{\alpha_{en}^2 + \beta_{en}^2}} \end{bmatrix}. \quad (S6)$$

In consideration of the demagnification of the projection system, the electric field in the exit pupil plane can be expressed as

$$E_{ex}(\alpha_{ex}, \beta_{ex}, \gamma_{ex}) = \frac{r_{en} \cdot \alpha_{en}}{r_{ex} \cdot \alpha_{ex}} \cdot \sqrt{\frac{\gamma_{in}}{\gamma_{ex}}} \cdot T_{ex} \cdot E_{en}. \quad (S7)$$

T_{ex} is the transformational matrix from local coordinates to the global coordinates in the image plane, which can be written as

$$T_{ex} = \begin{bmatrix} \frac{\beta_{ex}}{\sqrt{1 - \gamma_{ex}^2}} & \frac{\alpha_{ex} \cdot \gamma_{ex}}{\sqrt{1 - \gamma_{ex}^2}} \\ \frac{\alpha_{ex}}{\sqrt{1 - \gamma_{ex}^2}} & \frac{\alpha_{ex} \cdot \gamma_{ex}}{\sqrt{1 - \gamma_{ex}^2}} \\ 0 & \sqrt{1 - \gamma_{ex}^2} \end{bmatrix}. \quad (S8)$$

We can get the following expression for the electric field at the image plane after taking the inverse Fourier transform of the electric field at the exit pupil plane, i.e.,

$$E_{image}(x_i, y_i, z_i) = j \frac{n \cdot \alpha_{en} \cdot \exp(-j \cdot k \cdot r_{ex}) \cdot r_{ex}}{\lambda \cdot \alpha_{ex}} \cdot \iint E_{ex}(\alpha_i, \beta_i, \gamma_i) \cdot \exp(j \cdot 2\pi \cdot (f_p \cdot x_{image} + g_i \cdot y_{image})) \frac{d\alpha_{ex} \cdot d\beta_{ex}}{\gamma_{ex}} \cdot \quad (S9)$$

S3. Optical proximity correction method

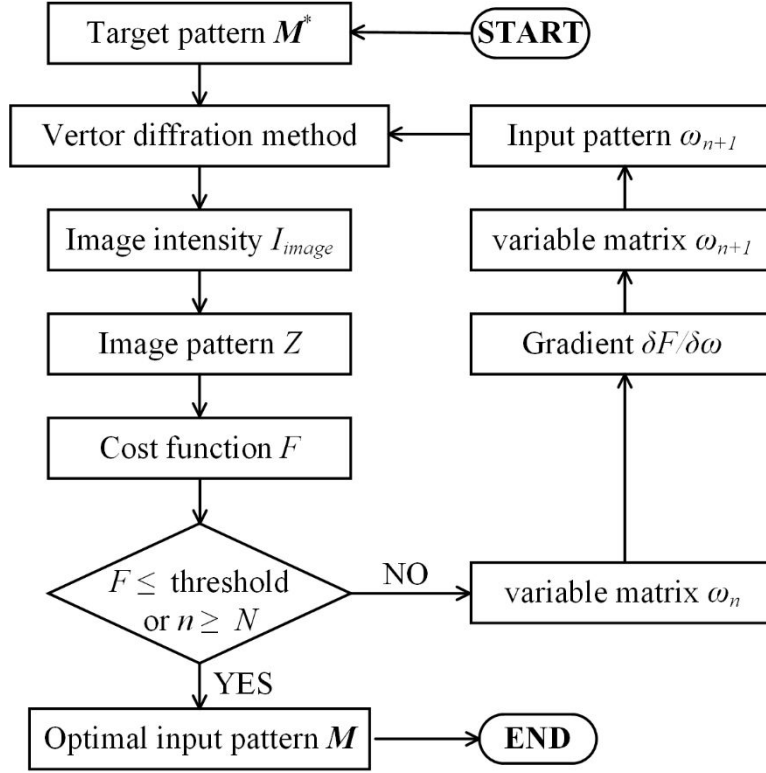


Figure S3 The flowchart of OPC algorithm.

In order to implement OPC algorithm, it is necessary to calculate the gradient of the cost function. To achieve this, the function of the projection system is extracted from the vector diffraction method. The function of the projection system is expressed as

$$H_p = \frac{2\pi}{n \cdot m} \int^{-1} (T_{g-g} \mathcal{W} \cdot E_{in}), \quad p = x_{in}, y_{in}, z_{in}. \quad (S10)$$

T_{ex} is the transformational matrix from the global coordinates in the input pattern plane to the global coordinates in the image plane, which can be written as

$$T_{g-g} = \begin{bmatrix} \frac{\beta_{ex}^2 + \alpha_{ex}^2 * \gamma_{ex}}{1 - \gamma_{ex}^2} & \frac{-\alpha_{ex} * \beta_{ex}}{1 + \gamma_{ex}} & \alpha_{ex} \\ \frac{-\alpha_{ex} * \beta_{ex}}{1 + \gamma_{ex}} & \frac{\alpha_{ex}^2 + \beta_{ex}^2 * \gamma_{ex}}{1 - \gamma_{ex}^2} & \beta_{ex} \\ -\alpha_{ex} & -\beta_{ex} & \gamma_{ex} \end{bmatrix}. \quad (S11)$$

The gradient of the cost function with respect to the input pattern then can be written

as

$$\begin{aligned}
\frac{\delta \|Z - M^*\|_2^2}{\delta M} &= 2 * \sum_{x,y} (Z - M^*) \cdot Z \cdot (1 - Z) \cdot \frac{\delta I_{image}}{\delta M} \\
&= 2a \cdot \sum_{x,y} (Z - M^*) \cdot Z \cdot (1 - Z) \cdot \frac{\delta (H \otimes M)^2}{\delta M} \\
&= 4a \cdot \text{Re} \left(\sum_{x,y} (Z - M^*) \cdot Z \cdot (1 - Z) \cdot (H \otimes M) \cdot \frac{\delta (H \otimes M)}{\delta M} \right) \quad (S12) \\
&= 4a \cdot \text{Re} \left(\sum_{x,y} (Z - M^*) \cdot Z \cdot (1 - Z) \cdot (H \otimes M) \cdot H(1-x, 1-y) \right) \\
&= 4a \cdot \text{Re} \left(H \otimes \left((Z - M^*) \cdot Z \cdot (1 - Z) \cdot (H \otimes M) \right) \right) \\
&= 2a \cdot \left(H \otimes \left\{ (Z - M^*) \cdot Z \cdot (1 - Z) \cdot (H \otimes M) \right\} \right)
\end{aligned}$$

The other steps for OPC (i.e., calculating image pattern, generating variable matrix, updating variable matrix and mask pattern) are shown in equation 2-7 in the mainbody.

S4. An application example of OPC

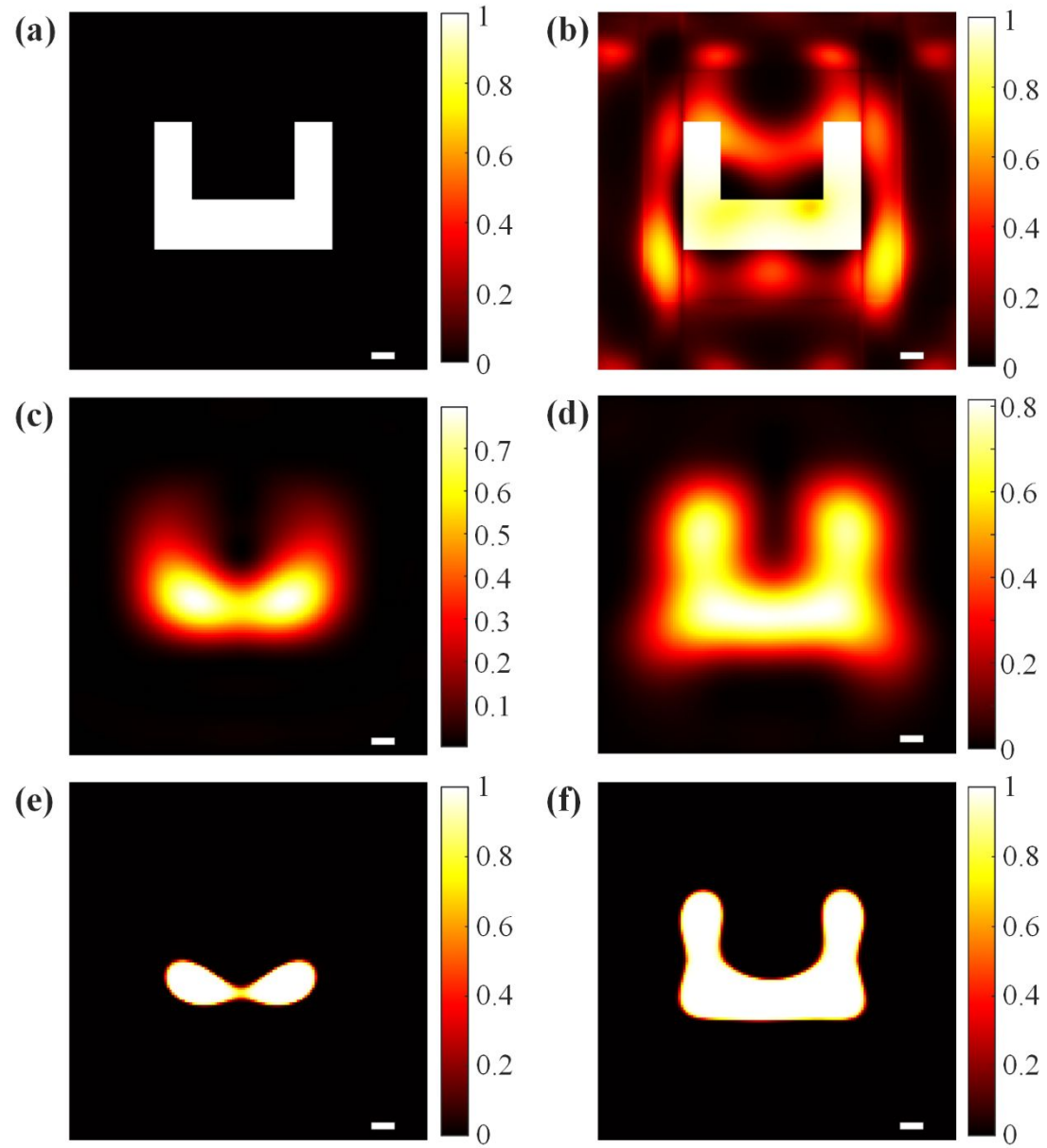


Figure S4 (a) The initial U-shape pattern, which is also the target pattern. (b) The optimal pattern after OPC. The optical images of (c) the initial and (d) the optimal pattern after projection. The wavelength is 421 nm and the NA is 0.95 in our simulation. (e) The imaging pattern calculated from (c) by using the Sigmoid function. (f) The imaging pattern calculated from (b) by using the Sigmoid function. In this simulation, the threshold and steepness of the Sigmoid function are 0.6 and 100, respectively. The pixel size of OPC is 10 nm in the image plane. Scale bar, 100 nm.

S5. The generated structured light field by OPC

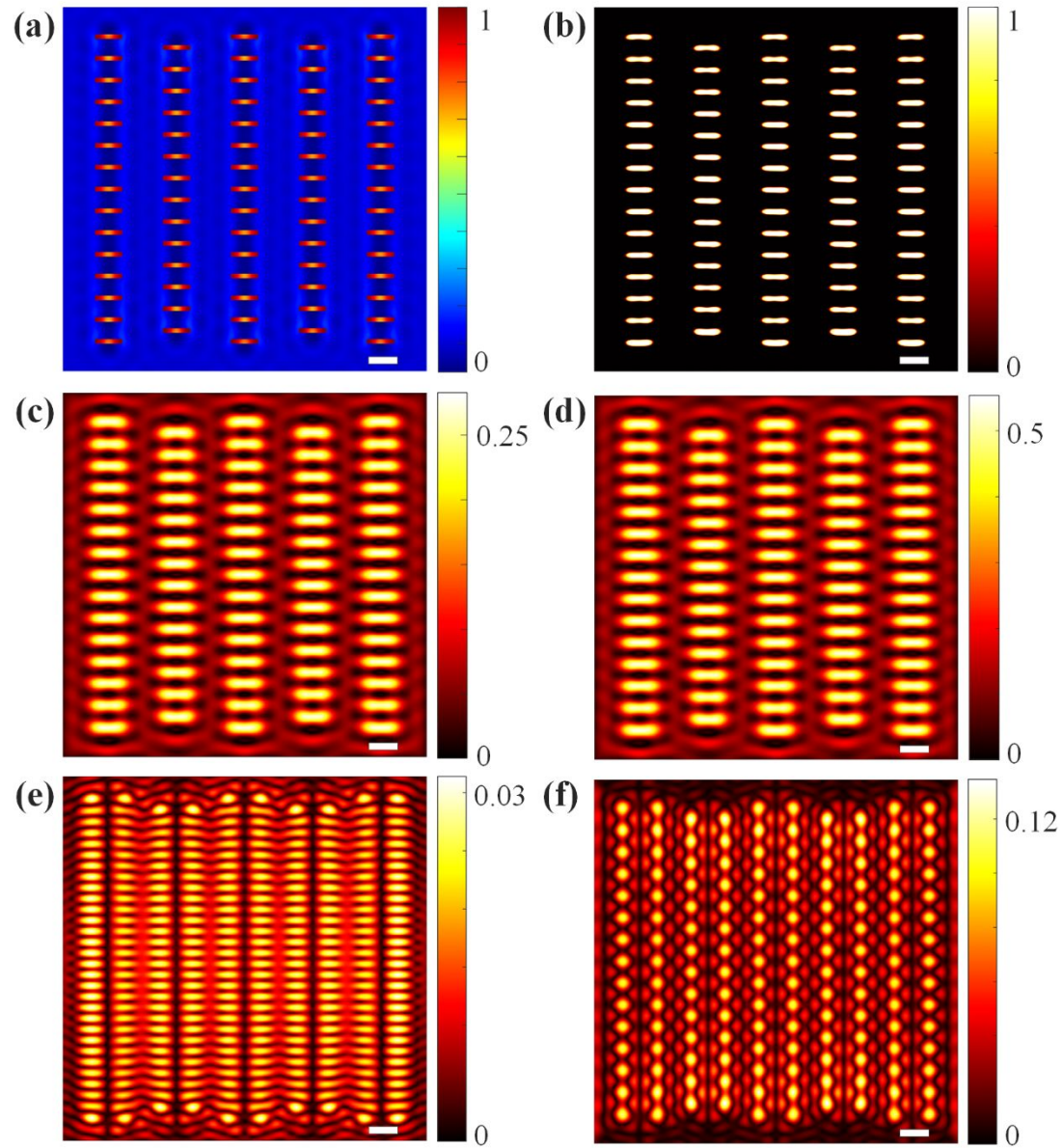


Figure S5 (a) The optimal pattern for the conjugate structured light field with a pixel size of 10 nm in the imaging plane, which can be loaded into the DMD or SLM in c-SIM. (b) The imaging pattern with a threshold of 0.2 and a steepness of 100. The imaging pattern match well with the tested pattern. (c) The intensity distribution of the generated conjugate structure light field that is generated by OPC for pattern (a) under the horizontal polarization state illumination. (d), (e), and (f) are the x , y , and z components of the electric field in the imaging plane, respectively. Scale bar, 500 nm.

S6. Optical inspection for three different types of defects

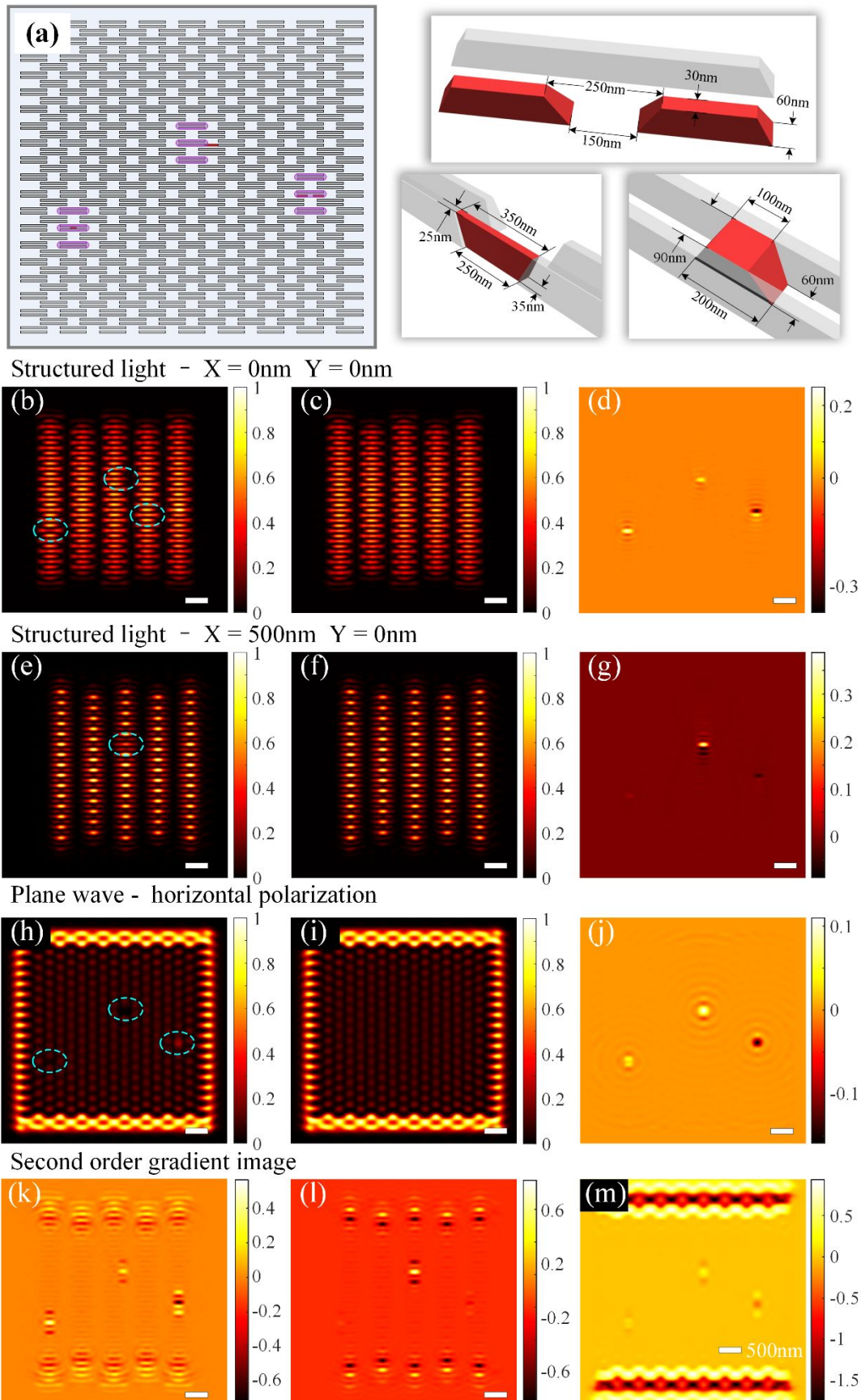


Figure S6 (a) The nanopattern with three different types of defects. The top width, top length, bottom width and bottom length of the Cutting defect are 30 nm (about $\lambda/14$), 250 nm, 60 nm and 150 nm, respectively. For Bx bridge defect, the dimensions are 25 nm (less than $\lambda/14$), 350 nm, 35 nm and 250 nm, respectively. As for By bridge defect, the dimensions are 90 nm, 100 nm, 60 nm and 200 nm, respectively. The heights of the three defects are the same as that of the background pattern, i.e. 100 nm. The images in the second row show the results of defect inspection using c-SIM, with structured light field illumination at the position of $x = 0$ nm, $y = 0$ nm. (b) The far-field image with defects. (c) The far-field image without defects. (d) The differential image between (b) and (c). The left and right perturbations are slightly stronger than the mid perturbation. The images in the third row show the results of defect inspection using c-SIM, with structured light field illumination at the position of $x = 500$ nm, $y = 0$ nm. (e) The far-field image with defects. (f) The far-field image without defects. (g) The differential image between (e) and (f). The mid perturbation is much stronger than the left and right perturbations. The fourth row of images show the results of defect inspection using plane wave illumination with horizontal polarization. (h) The far-field image with defects. (i) The far-field image without defects. (j) The differential image between (h) and (i). The left perturbation is slightly weaker than the other perturbations since the By bridge is relatively insensitive in the horizontal polarization illumination. (k) The second-order gradient image corresponding to structured light field illumination at the position of $x = 0$ nm, $y = 0$ nm. (l) The second-order gradient image corresponding to structured light field illumination at the position of $x = 500$ nm, $y = 0$ nm. (m) The second-order gradient image corresponding to plane wave illumination with horizontal polarization. There are abnormal perturbations in the upper and lower edges of the three gradient images, due to the shift in gradient calculation. As expected, the perturbations in second-order gradient images exhibit the same strength as the differential images and show the enhanced resolution effect.

S7. Optical far-field classification of two Cutting defects with opposite orientation

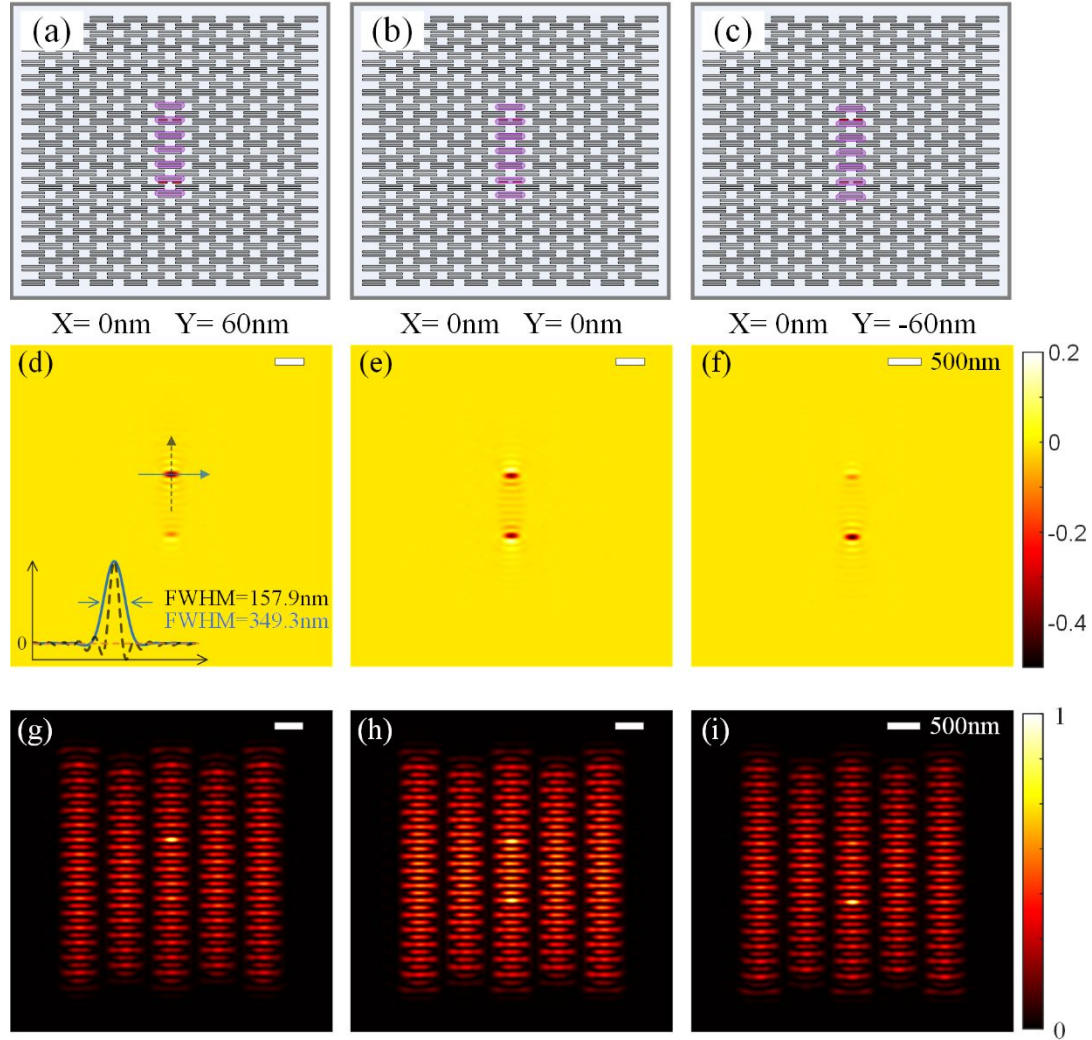


Figure S7 (a) The simulating nanopattern with a couple of axisymmetric Cutting defects set in a large-scale ideal nanopattern. The illuminating position of the structured light field is $x = 0 \text{ nm}$, $y = 60 \text{ nm}$. (b) and (c) use the same nanostructure as (a), but the illuminating position of the structured light field is $x = 0 \text{ nm}$, $y = 0 \text{ nm}$, and $x = 0 \text{ nm}$, $y = -60 \text{ nm}$, respectively. (d) The differential image at the illuminating position in (a), where the upper perturbation is stronger than the lower one. (e) The differential image corresponding to (b), where the two perturbations have similar strength. (f) The differential image corresponding to (c), where the lower perturbation is stronger than the upper one. The strength of those perturbations has the same characteristic as the second-order gradient image in Fig. 4. The far-field images depicted in (g), (h), and (i) correspond respectively (a), (b), and (c).

S8. Optical far-field classification of two Bx bridge defects with opposite orientation

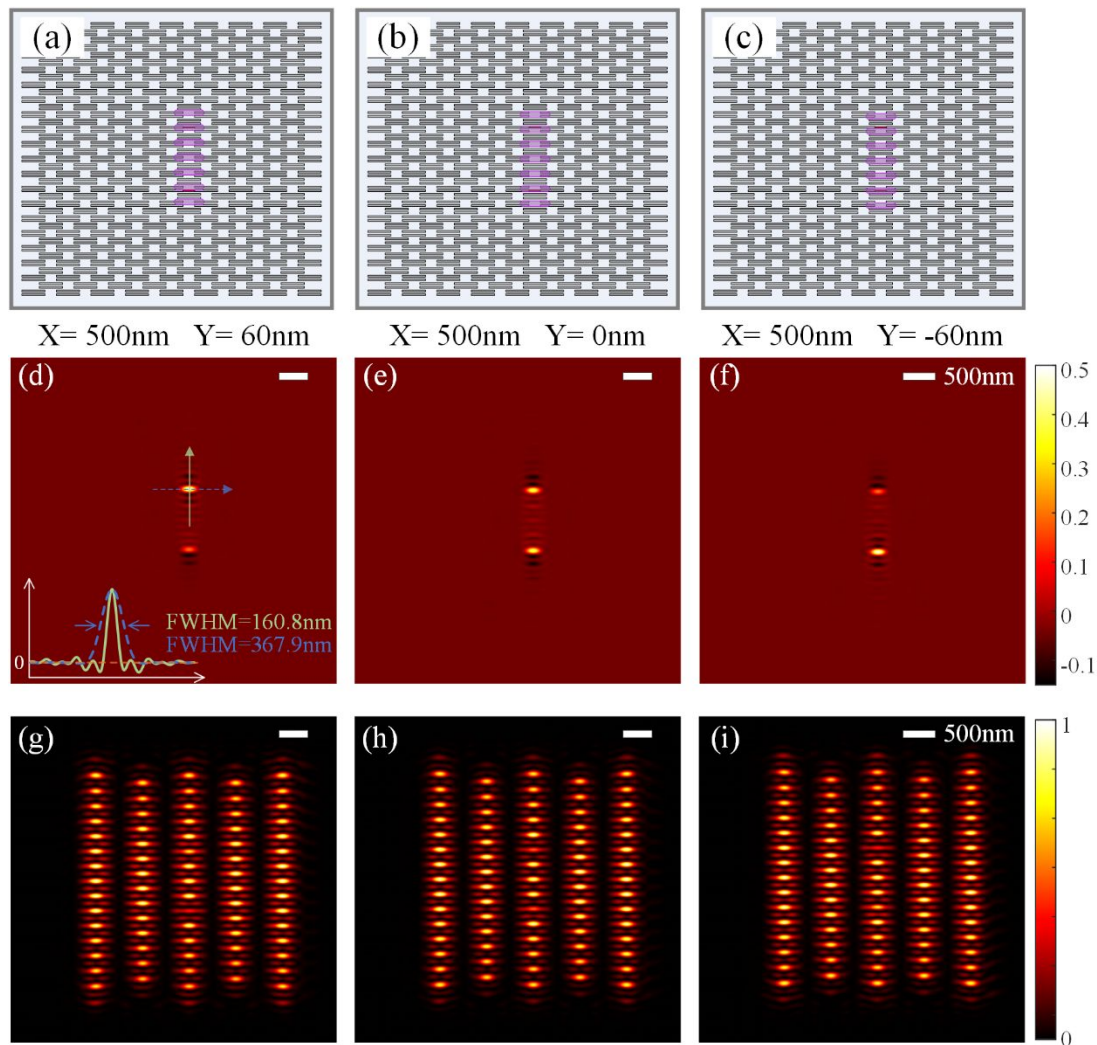
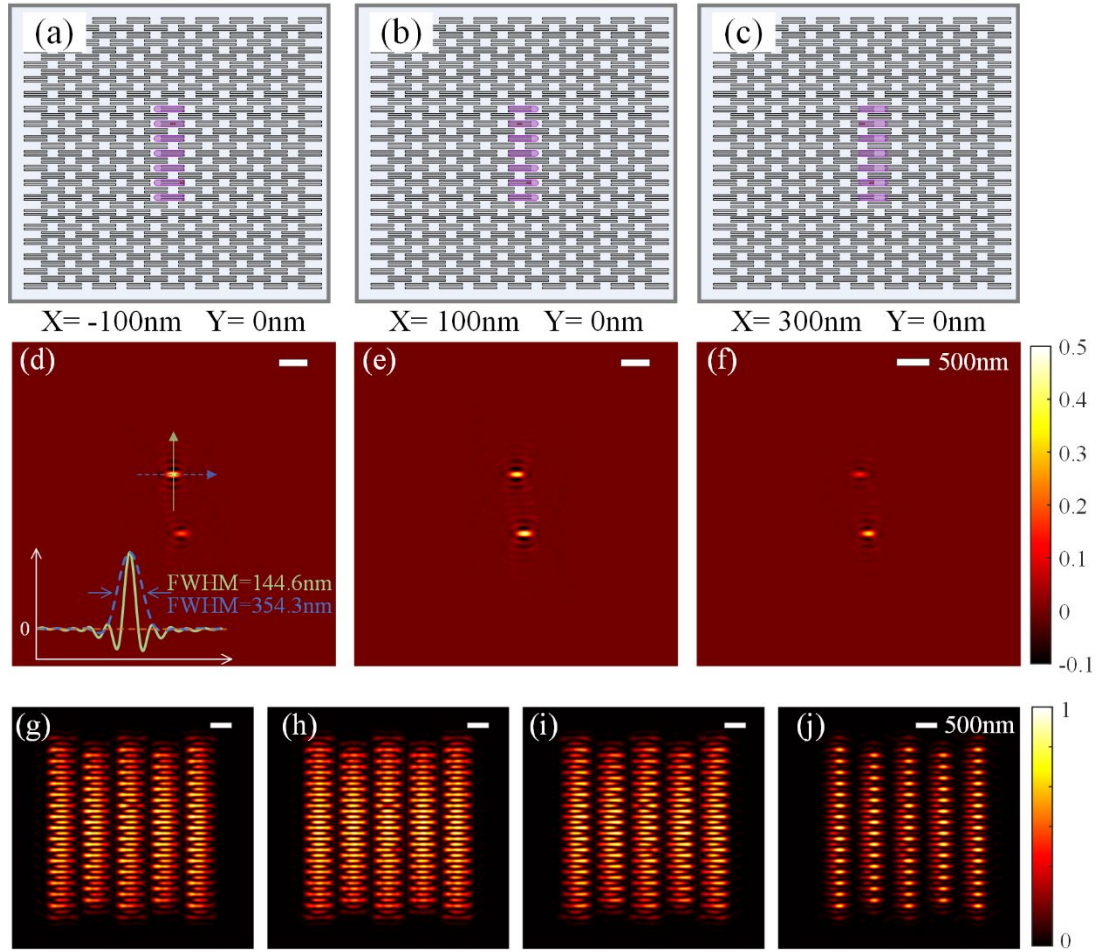


Figure S8 (a) The simulating nanopattern with a couple of axisymmetric Bx bridge defects set in a large-scale ideal nanopattern. The illuminating position of the structured light field is $x = 500$ nm, $y = 60$ nm. (b) and (c) is the same nanostructure as (a), but the illuminating position is $x = 500$ nm, $y = 0$ nm, and $x = 500$ nm, $y = -60$ nm, respectively. (d) The differential image at the illuminating position in (a), where the upper perturbation is stronger than the lower one. (e) The differential image corresponding to (b), where the two perturbations have similar strength. (f) The differential image corresponding to (c), where the lower perturbation is stronger than the upper one. The strength of those perturbations has the same characteristic as the second-order gradient image in Fig. 4. The far-field images depicted in (g), (h), and (i) correspond respectively (a), (b), and (c).

S9. Optical far-field classification of two By bridge defects with opposite orientation



S10. Defect localization precision

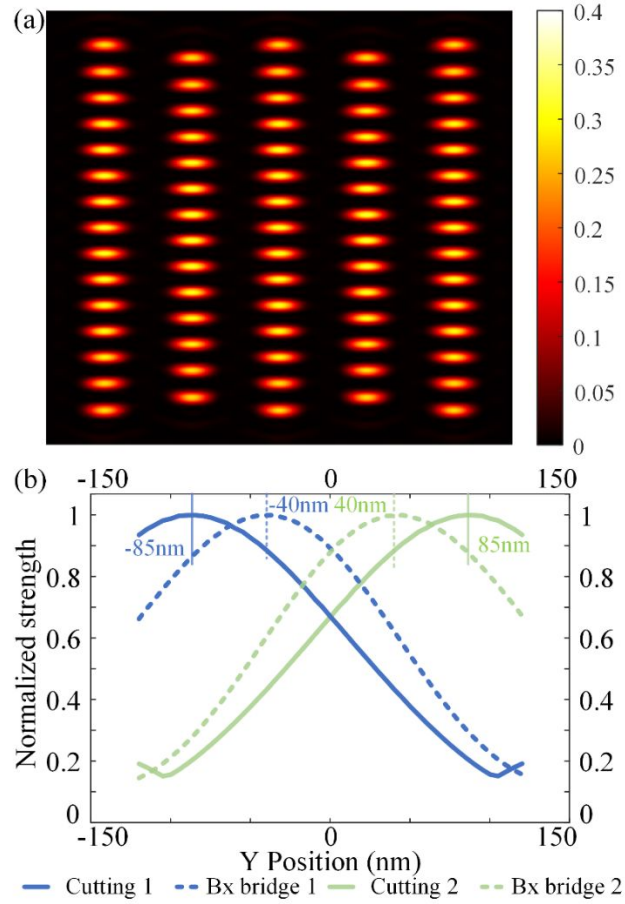


Figure S10 (a) Unoptimized structured light field. (b) The normalized far-field scattering signal of Bx bridge defects and Cutting defects as a function of the Y position of the scanning structure light field. Cutting 1 and Cutting 2 correspond to the lower and upper Cutting defects in S7, respectively. Bx bridge 1 and Bx bridge 2 correspond to the lower and upper Bx bridge defects in S8, respectively. The blue and green curves represent Defect 1 and Defect 2, respectively. The solid and dashed curves represent the Cutting defects and Bx bridge defects, respectively. The vertical lines mark the positions of the maximal value. The far-field scattering signals of two Cutting defects reach maximum at $Y = -85$ nm and 85 nm, respectively at a fixed position $X = 0$ nm. The far-field scattering signals of two Bx bridge defects reach maximum at $Y = -40$ nm and 40 nm, respectively at a fixed position $X = 500$ nm. Because Cutting defects and Bx bridge defects break the symmetry of the local structure and induce off-axis scattering, the positions of the strongest far-field scattering signals induced by the four defects deviate from the physical center of the defects, which are 60 nm or -60 nm.